

The impact of gas bulk rotation on the Lyman- α line

Nicolas Garavito-Camargo¹, Jaime E. Forero-Romero¹ and Mark Dijkstra²

¹*Departamento de Física, Universidad de los Andes, Cra. 1 No. 18A-10, Edificio Ip, Bogotá, Colombia*

²

16 August 2013

ABSTRACT

Rotation is present in the gas kinematics of galaxies up to the highest redshifts. In this paper we present for the first time radiative transfer calculations that show the impact of gas bulk rotation on the morphology of the Lyman α line. To this end we model a galaxy as an homogeneous sphere composed as an homogeneous mixture of dust and hydrogen at a constant temperature. These spheres have a solid-body rotation with linear velocities at the surface in the range $0 - 300 \text{ km s}^{-1}$ and neutral hydrogen optical depths in the range $\tau_{\text{H}} = 10^5 - 10^7$. We consider radiation sources both in the center of the rotating cloud and also homogeneously distributed in the volume. We find that higher rotational velocities increase the width of each peak in the outgoing line profile while it also increases the amount of Lyman alpha photons escaping in the line center. This trends makes that for high rotational velocities and large Hydrogen optical depths the double peak of the line tends to be erased and be replaced by a single peak at the line center. This trend is more pronounced for radiation sources homogeneously distributed. Concerning the escape fraction we find that rotation does not have any effect, provided that all the sources are centrally emitted. However, in the case of homogeneously emitted sources we measure an increase of about a factor of 2 in the escape fraction for higher rotational velocity values. This work shows that gas bulk rotation has a non negligible impact on the shape of the Lyman α line.

Key words: galaxies: high-redshift - galaxies: star formation - line: formation

1 INTRODUCTION

[Due to the resonant nature of the Lyman alpha line, gas kinematics play an important role shaping its morphology.]

[Line morphology is being measured observationally.]

[There is an extensive literature studying the influence of outflow/inflow configurations in the shape of the outgoing Lyman-alpha line.]

[Rotation is present in high redshift galaxies.]

In this paper we study for the first time the impact of rotation on the morphology of the Lyman α line. To isolate the effects of rotation we focus on a simple system: the gas distribution is spherical, with homogeneous density and the gas rotates as a solid body. We base our work on two independent Monte Carlo based radiative transfer codes CLARA (Forero-Romero et al. 2011) and XX (Dijkstra & Kramer 2012).

This paper is structured as follows...

In this paper we express a photon's frequency in terms of the dimensionless variable $x \equiv (\nu - \nu_{\alpha})/\Delta\nu_{\alpha}$, where $\nu_{\alpha} = 2.46 \times 10^{15} \text{ Hz}$ is the Ly α resonance frequency, $\Delta\nu_{\alpha} \equiv \nu_{\alpha} \sqrt{2kT/m_p c^2} \equiv \nu_{\alpha} v_{\text{th}}$ is the doppler broadening of the line which depends on the neutral gas temperature T

scattering the radiation or equivalently the thermal velocity v_{th} of the atoms.

2 MODELING BULK GAS ROTATION

Describing the kinematics of gas rotation in all generality is a complex task, specially at high redshifts where there is still missing a thorough observational account of rotation in galaxies beyond $z > 1.0$. Furthermore, at low redshifts it has been observed a great variation in the shape of the rotation curve as observed in HI emission as a function of the distance to the galaxy center. However there are two features that are observed very often. First, in the central region the velocity increases proportional to the radius, following the behaviour in a body with solid rotation. Second, beyond a certain radius the rotation curve tends to flatten.

An ab-initio description of realistic rotation curves in simulations depends on having access to the dynamic evolution of all mass components in the galaxy: stars, gas and dark matter. Such level of realism is extremely complex to achieve, specially if one wants to get a systematic description based on statistics of simulated objects.

Following the tradition of studies of Lyman α emitting

systems, we implement a model with a simplified geometry and gas distribution. We assume that the gas is homogeneously distributed in a sphere that rotates as a solid body with constant angular velocity. This simple model will contain only one parameter: the linear velocity at the sphere's surface, V_{\max} .

2.1 Detailed Implementation of Rotation

In the MonteCarlo code we define a cartesian coordinate system to define the position of each photon. The origin of this system coincides with the center of the sphere and the rotation axis is defined to be z -axis. With this choice, the components of the gas bulk velocity field, $\vec{v} = v_x\hat{i} + v_y\hat{j} + v_z\hat{k}$, can be written as

$$v_x = -\frac{y}{R}V_{\max}, \quad (1a)$$

$$v_y = \frac{x}{R}V_{\max}, \quad (1b)$$

$$v_z = 0, \quad (1c)$$

where R is the radius of the sphere and V_{\max} is the linear velocity at the sphere's surface. The minus/plus sign in the x/y -component of the velocity indicates the direction of rotation. In this case we take the angular velocity in the same direction as the \hat{k} unit vector. With these definitions we can write the angular velocity as $\omega = V_{\max}/R$.

In contrast with spherically symmetric models (static, outflow, inflow) the rotation now defines a preferred direction in the problem. In Section 3 we quantify this differences by varying the line of sight of a mock observer with respect to the rotation axis. The results are parametrized by the polar angle θ as defined by the dot product $\cos\theta = \hat{u} \cdot \hat{k}$.

2.2 Grid of Simulated Galaxies

In the Monte Carlo calculations we follow the propagation of $N_\gamma = 10^5$ numerical photons through different spherical galaxies. Each galaxy model varies at least one of the following parameters: the maximum rotational velocity V_{\max} , the hydrogen optical depth τ_H , the dust optical depth τ_a and the initial distribution of photons with respect to the gas. There are in total 60 models combining all the input parameters summarized in Table 1.

We have used two independently developed Monte Carlo codes (Forero-Romero et al. 2011; Dijkstra & Kramer 2012) to perform the calculations of the non-dusty models. The results we report here are robust in the sense that they are obtained by both codes.

3 RESULTS

The central result of this paper is summarized in Fig. 1 that shows clearly the considerable impact of rotation on the morphology of the emergent Ly α line. Both panels in the Figure focus on the results for $\tau_H = 10^7$, showing that the influence of rotation is present both when the photons are either homogeneously or centrally initialized over the gas volume.

In the following subsections we characterize the line

Physical Parameter (units)	Symbol	Values
Velocity (km s^{-1})	V_{\max}	0, 50, 100, 200, 300
Hydrogen Optical Depth	τ_H	$10^5, 10^6, 10^7$
Dust Optical Depth	τ_a	0,1
Photons Distributions		Central, Homogeneous

Table 1. List of the physical parameters that define the spherical models imulated using Monte Carlo calculations. For each parameter we vary the values in the range listed in the last column. Takig into account all the possible combinations we end up with 60 different models.

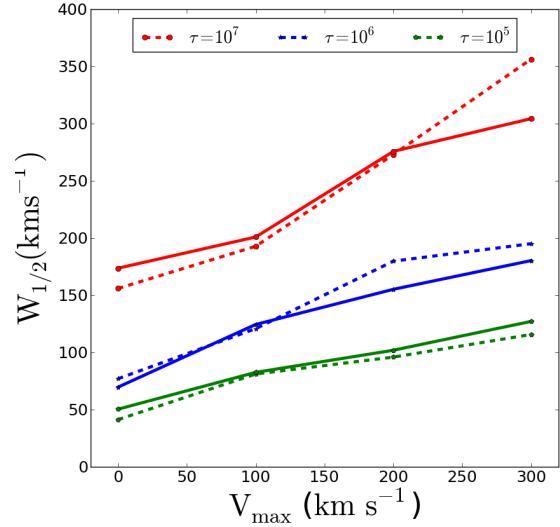


Figure 2. Half-width for the non-dusty models as a function of rotational velocity V_{\max} . Continuous (dashed) lines correspond to homogeneous (central) source distributions.

morphology by the half-width at half intensity and the peak maxima. In order to interpret the morphological changes in the line we also report the median number of scatter for each Ly α photon in the simulation. Finally we measure the bulk escape fraction as a function of rotational velocity in the presence of dust.

All the results in this section are constructed by taking into account all outgoing photons regardless of the direction of propagation. In the next section ?? we quantify the changes in the observed spectra for observers with different viewing angles.

3.1 Line width and peak maxima

The first quantitative conclusion of the effect of rotation in the Ly α line is that double peaks broaden and reduce their intensity while the line center rises. This produces the impression that, as the rotational velocity increases, the double peaks are merged into a single broad emission peak. This is most evident in the highest rotational velocities for the homogeneously distributed sources (right panel in Fig. 1).

To quantify the line broadening we use a modified version of the full width at half maximum (FWHM). We mea-

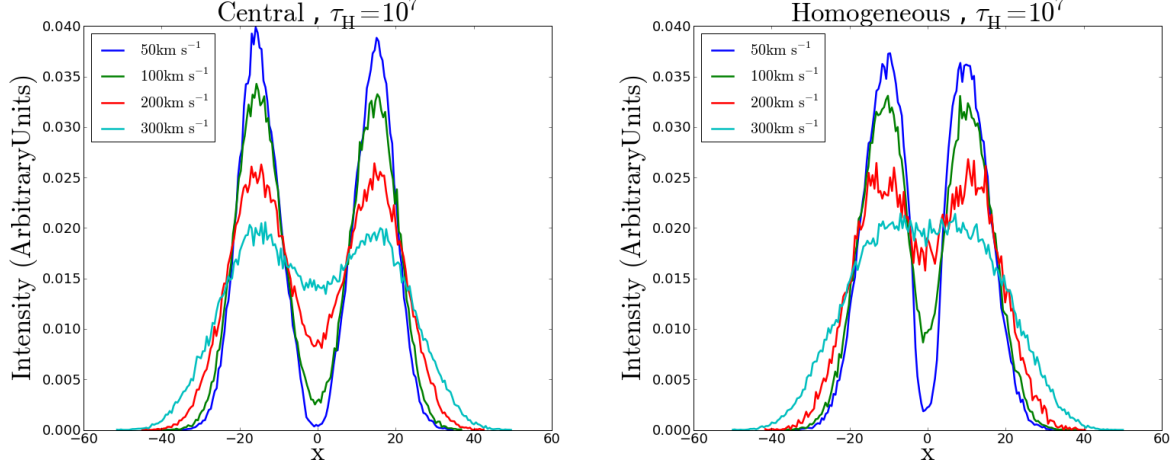


Figure 1. Shape of the Ly α line for different velocities rotational velocities for spherical distributions with $\tau_H = 10^7$. The left (right) panel shows the central (homogeneous) photon distribution. All photons were taken into account regardless of their propagation direction.

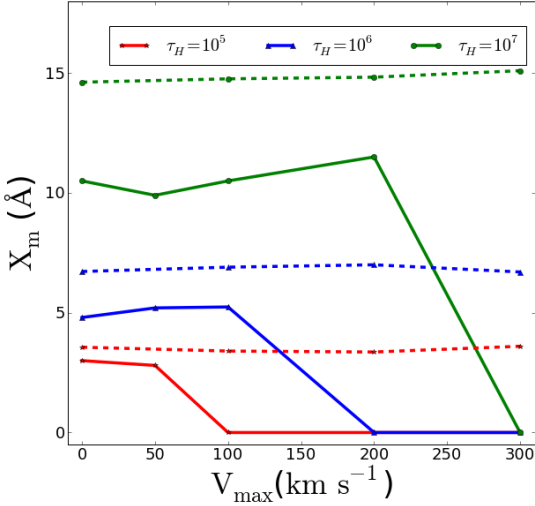


Figure 3. Position of the peak maxima as a function of rotational velocity V_{\max} . Continuous (dashed) lines correspond to homogeneous (central) source distributions. A value of $x_{\max} = 0$ indicates that line becomes single peaked.

sure it only for half of the line, $W_{1/2}$. This definition allows us to quantify the line width and see the transition from double to single peak emission. In the case of double peaked emission $W_{1/2}$ corresponds to the width of a single peak, while in the extreme case of high rotational velocities, when the double peak is erased, it simply correspond to half FWHM.

Figure 2 shows how $W_{1/2}$ increases with rotational velocity. Continuous (dashed) lines connect the results for homogeneous (central) source distribution. The line width increases with rotational velocity up to factors of ~ 2 at 300 km s^{-1} with respect to the static case. For the temperature $T = 10^4 \text{ K}$ used in our radiative transfer calculations

the thermal velocity is $v_{th} = 12.8 \text{ km s}^{-1}$. For a model with τ_H it means that the half-width can increase up to 350 km s^{-1} (at $V_{\max} = 300 \text{ km s}^{-1}$) compared to a half-width of 150 km s^{-1} in the static case.

Figure 3 shows the position for the peak maxima as a function of the rotational velocity V_{\max} . This Figure shows us clearly that in the case of central distributed sources there is barely any change with rotational velocity in the range of explored parameters. However, in the case of homogeneously emitted sources the maxima position remain close to constant until beyond some velocity threshold the line becomes single peaked with $x_{\max} = 0$.

The transition to a single peak line occurs for systems where it becomes easier for the bulk of the photons to escape with the lowest number of scatterings possible, allowing them not to move very far from the center of the line. This explains how the single peak stage is easily achieved in the homogeneous source distribution. In this case there is a fraction of the photons that are inside a photosphere region with $\tau_{H,r} \ll \tau_H$ where $\tau_{H,r}$ is the optical depth from the radius of emission to the sphere's surface. This conditions allows the photons to escape with much less scatterings compared to the photons emitted at the very center of the sphere. In turn, it gives the photons less scatterings to be placed far from the line center. Increasing the rotational velocity V_{\max} reduces the optical depth making the photosphere region effectively larger, increasing the number of photons escaping close to the lines's center. For the central case the photosphere is not present, and other mechanisms must be at play in the steady reduction of the double peak.

For larger values of τ_H the transition to a single peaked emission occurs for larger values of the rotation velocity. In our models we find the following correspondence between the optical depth $\tau_H = \{10^5, 10^6, 10^7\}$ and the transitional velocities $V_{\text{trans}} = \{50 - 100 \text{ km s}^{-1}, 100 - 200 \text{ km s}^{-1}, 200 - 300 \text{ km s}^{-1}\}$ which can only be constrained to be in the range of velocities in the models that gave a $x_{\max} \neq 0$ and $x_{\max} = 0$. In the next section explore the origin of this trends

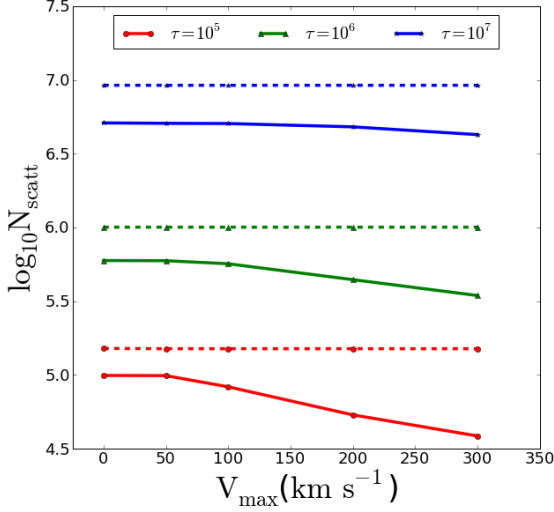


Figure 4. Logarithm of the average number of scatterings as function of the velocity.

and show to what extent a low number of scatterings is correlated with the emergence of a single peak.

3.2 Average Number of Scatterings

The number of times that a Ly α photon is absorbed and re-emitted is connected to the final frequency that it can have after escaping the galaxy. In the case of static gas geometries, a large value of the optical depth is immediately followed by a high number of scatterings. In turn a large optical depth increases the probability that a Ly α photon to be found far from the center of the line. In this case, the peak maxima shift away from the line center as the amount of neutral hydrogen increases.

In Figure 4 we show the average number of scatterings $\langle N_{\text{scatt}} \rangle$ as a function of the rotational velocity V_{max} . For the central distributions we find that there is not a significant change for increasing rotational velocities, $\langle N_{\text{scatt}} \rangle$ changes less than 0.5% for different velocities. In this case we also find that the average number of scatterings is proportional to the optical depth, as expected in analogy from the analytic result for the homogeneous infinite-slab $\langle N_{\text{scatt}} \rangle = 1.612\tau_{\text{H}}$ (Adams 1972; Harrington 1973). In our experiments we find that for the static spheres with centrally distributed sources $\langle N_{\text{scatt}} \rangle = (1.50, 1.00, 0.92)\tau_{\text{H}}$. for optical depths $\tau_{\text{H}} = (10^5, 10^6, 10^7)$

Figure 4 shows that for the homogeneous distribution there is a clear decrease of $\langle N_{\text{scatt}} \rangle$ as the V_{max} increases. This effect more pronounced for the lower values of the optical depth. For $\tau_{\text{H}} = 10^5$ the average number of scatterings decreases by 61% at $V_{\text{max}} = 300 \text{ km s}^{-1}$ in comparison to the static case.

The analytic expectation for the slab with homogeneously emitted sources is $\langle N_{\text{scatt}} \rangle = 1.16\tau_{\text{H}}$ (Harrington 1973), a factor of 0.72 lower than the case of the centrally emitted photons. In our case we find that for the static, while for homogeneously distributed source $\langle N_{\text{scatt}} \rangle = (1.50, 1.00, 0.92)\tau_{\text{H}}$. **seguro ????**

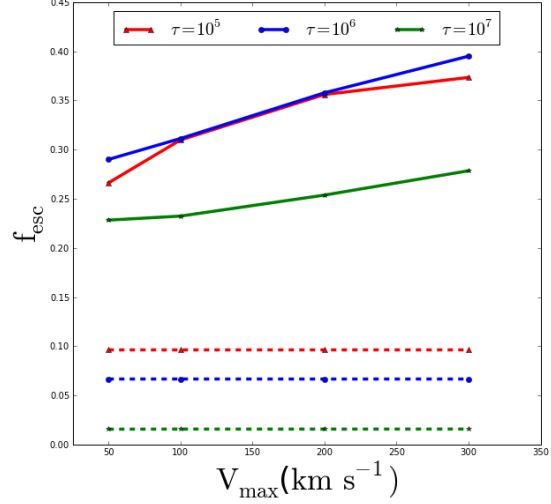


Figure 6. Escape fraction as a function of rotational velocity. The continuous (dashed) lines correspond to homogeneous (central) models.

In order to gain a deeper understanding of these results we prepare 2D histograms for the number of scatterings as a function of the outgoing dimensionless frequency x . In Figure 5 we show the results of such histogram in the case $\tau_{\text{H}} = 10^5$ for the static case and $V_{\text{max}} = 300 \text{ km s}^{-1}$. The upper (lower) panels show the results for the homogeneous (central) source distribution. The color scale is logarithmic in the number of photons at a certain value $x - N_{\text{scatt}}$. This Figure clearly support our hypothesis about the photosphere in the homogeneous distribution, in this case most of the photons that left with $x \sim 0$ have escaped with less than 10 scatterings, clearly explaining the origin of a single central peak. However, for a central distribution the situation is different. In this case the number of scatterings remains high, on the order of the optical depth, but the two peaks do get closer to each other. In this situation each scattering leaves the photon closer to the center of the line than the static case.

3.3 Dusty Clouds: Escape Fraction

We also study a dusty cloud configuration to measure the effect of rotation on the escape fraction. We expect that the modified number of scatterings to be reflected in this amount of photons absorbed by dust. Following this line of thought, we do not expect any change in for a dusty cloud with central source of radiation given that the number of scatterings remains close to constant. On the other hand, in the case of an homogeneous radiation source the number of scatterings drops as V_{max} increases, which might be reflected as an increasing escape fraction.

Figure 6 shows the dependence of the escape fraction as a function of the maximum rotational velocity, confirming that our intuitions in this respect is correct. For the central source distribution the escape fraction barely shows any change, while for the homogeneous case there is a clear rise in the escape fraction for high rotational velocities. Ro-

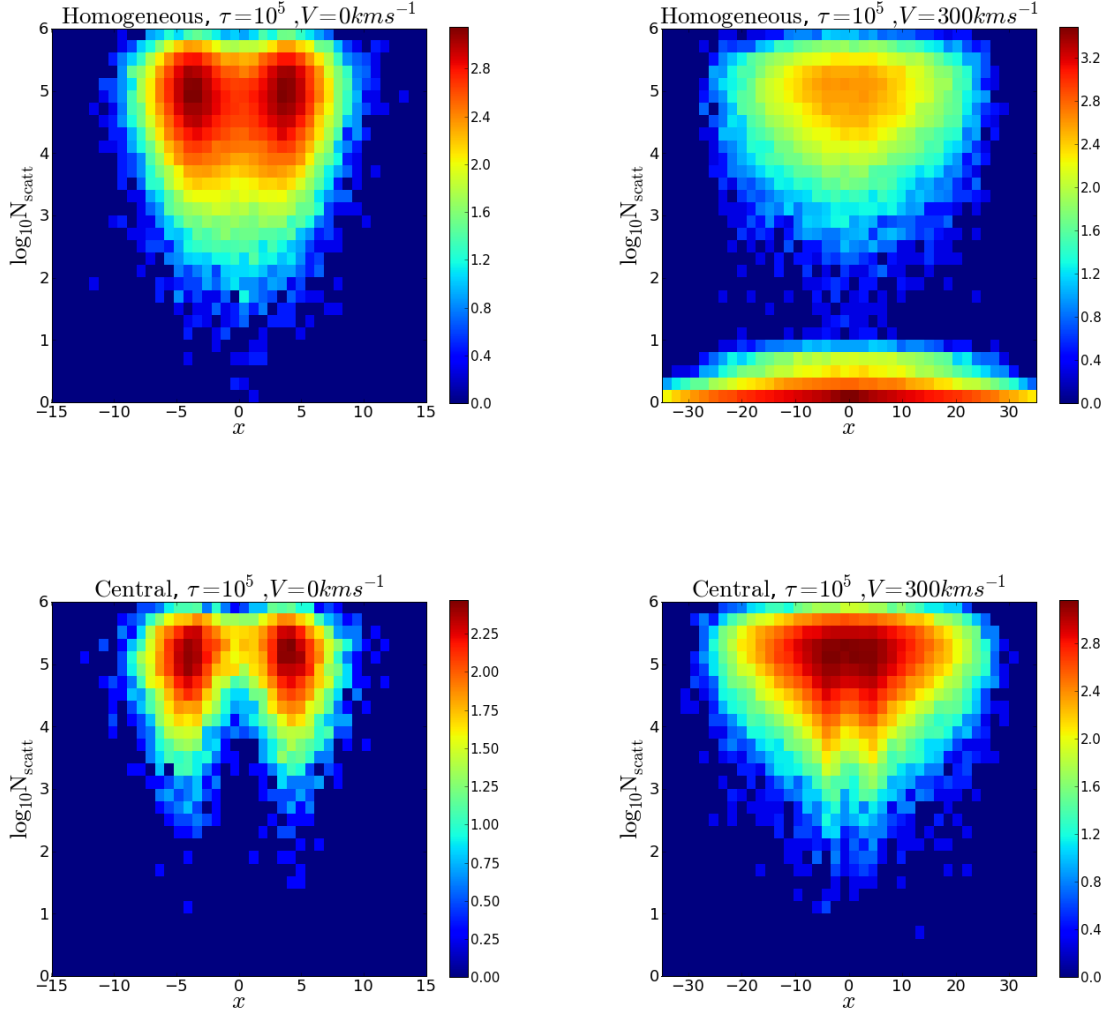


Figure 5. 2D histogram of N_{scatt} vs x . The upper (lower) pannels show the homogeneous (central) source distribution. Left corresponds to the static case and the right $V_{\text{max}} = 300 \text{ km/s}$. The colour scale is logarithmic on the number of photons with given values of N_{scatt} and x .

tation has a higher relative impact in the models with low optical depth $\tau_{\text{H}} = 10^5, 10^6$, where it can raise from xxx in the static case up to xxx at $V_{\text{rot}} = 300 \text{ km s}^{-1}$.

In Figure 7 we put these results in the context of the analytical solution for the infinite slab (Neufeld 1990). In Neufeld's setup the analytic solution depends solely on the product $(a\tau_{\text{H}})^{1/3}\tau_a$, an approximation that is valid only in the limits $a\tau_{\text{H}} \gg 1$. The dashed lines in Figure 7 correspond to the cases of different velocities. We observe that the escape fraction is higher by factors of 2 – 10 than the expected values for the slab configuration. We also see that for the lower value $\tau_{\text{H}} = 10^5$ the escape fraction does not increase with respect to the solution for $\tau_{\text{H}} = 10^6$ as expected, however we not that we are in a regime where the condition for the analytic expectations ($a\tau_{\text{h}} \gg 1$) does not hold.

3.4 Different line of sights

3.5 Off-Centered emission

4 DISCUSSION

... Comparison with Verhamme et al. results on the rotation

... Compare with Kulas et al (Figure 3), Rotation on the lyman alpha line convert double peak profiles into a single one. comments about rotation with inflows and outflows.

... The results derived in this paper have consequences on the interpretation of galaxy observations in the Lyman alpha line.

..compare steidel et al (2011)

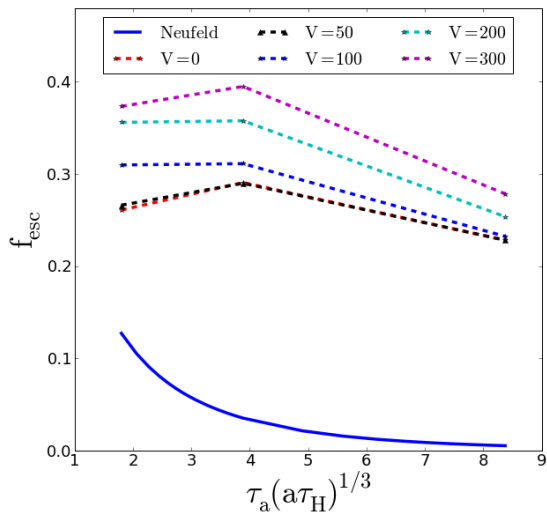


Figure 7. Escape fraction as a function of the product $(a\tau_H)^{1/3}\tau_a$. The analytic solution for the infinite slab is shown as a continuous line. Different dashed lines correspond to different rotational velocities.

5 CONCLUSIONS

In this paper we have estimated the effects of gas bulk rotation on the emission of the Lyman α line. We based the study on the study of a simplified configuration of an homogeneous sphere rotating as a solid body. We explored a range of models by varying the rotation speed, hydrogen optical depth, dust optical depth and initial distribution of Ly α photons with respect to the gas density. This was implemented in CLARA, a Monte-Carlo radiative transfer code already used to study the Lyman α line.

As first we see how the width of the line changes using a modified FWHM explained in section 3.1, and we found that as gas bulk rotation increase also the width increase in a factor of 2 – 3 in comparison with the static case. We also take into account the influence of the observer viewing angle, we found that observers with a line of sight perpendicular to the axis of rotation measure a 15% larger line width than those aligned with the rotation axis.

As many observational spectra Ly α emission line (Kulas et al) is double peaked, these peaks provide important information concerning gas kinematics and geometry, which can be partially explained with inflows/outflows of gas content. We study the effect of rotation in the position of this peaks, and we find that the position of the maxima does change with rotation for the homogeneous models when the double peak merged into a single peak as velocity increase. This effect is not seen for the central distribution when the double peak remains constant as the velocity increase. We also find that there is no dependency in the observer viewing angle with the maxima position.

Concerning the escape fraction under rotational effects on the Ly α emission line, we found that the escape fraction increase in about 20% – 30% for the homogeneous sphere model. While rotational effects are negligible for the central models and the escape fraction remains constant. Also the observer viewing angle have no effect in the escape frac-

tion neither for the homogeneous and central models. Complementing this analysis we study the average number of scatterings $\langle N_{scatt} \rangle$ that photons perform before escaping of the cloud taking into account rotational effects. The main result here is for the homogeneous models for which as velocity increase photons escape with about $\sim 39\%$ less scatterings than in the static case.

As an application of these results we compute the integrated flux taking into account the narrow band filters used by (Steidel et al 2011), for our models we found an important decrease up to 40% for the homogeneous models, and up to 22% for the dusty homogeneous models in the flux as velocity increase. Also we calculate at what redshift should the filter be in order to get the maximum flux, and for the three filters we get values that rely in the filter redshift range. This effects would have a relevant implication at the time to find high redshift galaxies.

This paper illustrates for the first time the main effects of rotation in the morphology of the Ly α emission line, we estimate the range of this effects for simplified models.

ACKNOWLEDGEMENTS

REFERENCES

- Adams T. F., 1972, ApJ, 174, 439
- Dijkstra M., Kramer R., 2012, MNRAS, 424, 1672
- Forero-Romero J. E., Yepes G., Gottlöber S., Knollmann S. R., Cuesta A. J., Prada F., 2011, MNRAS, 415, 3666
- Harrington J. P., 1973, MNRAS, 162, 43
- Neufeld D. A., 1990, ApJ, 350, 216

APPENDIX A: TABLES